

Accepted Manuscript

Point defect structure of La-doped SrTiO₃ ceramics with colossal permittivity

Mengjie Qin, Feng Gao, Jakub Cizek, Shengjie Yang, Xiaoli Fan, Lili Zhao, Jie Xu, Gaogao Dong, Mike Reece, Haixue Yan



PII: S1359-6454(18)30817-6

DOI: [10.1016/j.actamat.2018.10.025](https://doi.org/10.1016/j.actamat.2018.10.025)

Reference: AM 14903

To appear in: *Acta Materialia*

Received Date: 24 May 2018

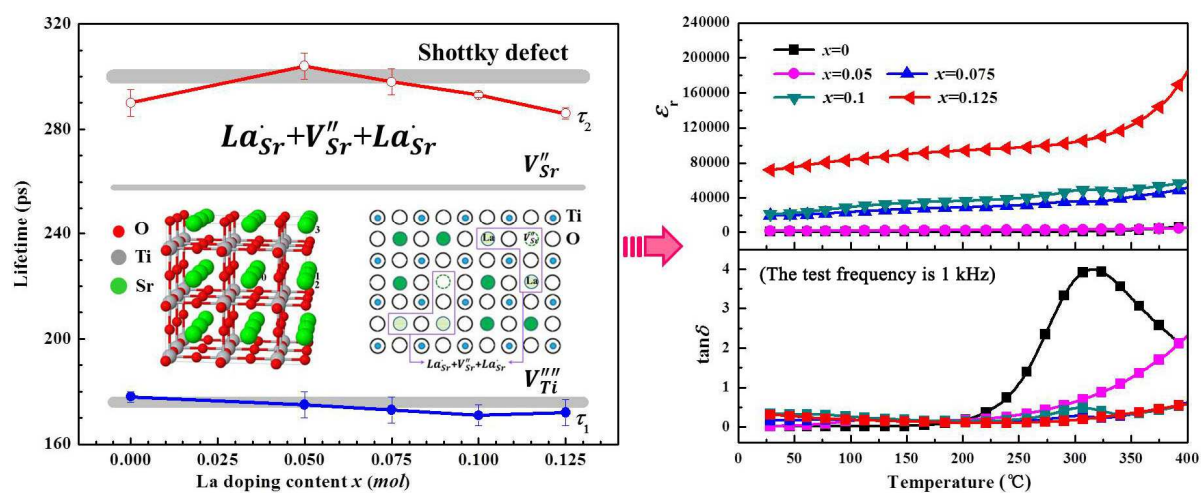
Revised Date: 3 October 2018

Accepted Date: 11 October 2018

Please cite this article as: M. Qin, F. Gao, J. Cizek, S. Yang, X. Fan, L. Zhao, J. Xu, G. Dong, M. Reece, H. Yan, Point defect structure of La-doped SrTiO₃ ceramics with colossal permittivity, *Acta Materialia* (2018), doi: <https://doi.org/10.1016/j.actamat.2018.10.025>.

This is a PDF file of an unedited manuscript that has been accepted for publication. As a service to our customers we are providing this early version of the manuscript. The manuscript will undergo copyediting, typesetting, and review of the resulting proof before it is published in its final form. Please note that during the production process errors may be discovered which could affect the content, and all legal disclaimers that apply to the journal pertain.

Graphical Abstract



Point defect structure of La-doped SrTiO₃ ceramics with colossal permittivity

Mengjie Qin^{1,4}, Feng Gao^{1,4*}, Jakub Cizek², Shengjie Yang¹, Xiaoli Fan^{1,4}, Lili Zhao³, Jie Xu^{1,4},

Gaogao Dong¹, Mike Reece^{4,5}, and Haixue Yan^{4,5}

1 State Key Laboratory of Solidification Processing, MIIT Key Laboratory of Radiation Detection Materials and Devices, USI Institute of Intelligence Materials and Structure, School of Material Science and Engineering, Northwestern Polytechnical University, Xi'an, 710072, China

2 Department of Low-Temperature Physics, Faculty of Mathematics and Physics, Charles University, Prague, 18000, Czech Republic

3 School of Information and Technology, Northwest University, Xi'an, 710127, China

4 NPU-QMUL Joint Research Institute of Advanced Materials and Structure, Northwestern Polytechnical University, Xi'an, 710072, China

5 School of Engineering and Materials Science, Queen Mary University of London, London, E1 4NS, United Kingdom

The e-mail address of each author:

qinmengjie_2014@126.com, gaofeng@nwpu.edu.cn, jcizek@nbox.troja.mff.cuni.cz,

976210201@qq.com, xlfan@nwpu.edu.cn, zhao_lili1109@163.com, xujie@nwpu.edu.cn,

643888535@qq.com, m.j.reece@qmul.ac.uk, h.x.yan@qmul.ac.uk

* Corresponding author

E-mail: gaofeng@nwpu.edu.cn Tel: +86-29-88492642

Abstract:

$\text{Sr}_{1-x}\text{La}_x\text{TiO}_3$ (SLTO) ceramics with colossal permittivity were fabricated by conventional solid-state reaction method. The point defects of pure STO and SLTO ceramics were analyzed by Positron Annihilation Lifetime Spectroscopy (PALS) and Coincidence Doppler Broadening (CDB). The charge compensation mechanisms and dielectric properties of ceramics were investigated. The results indicated that the intrinsic defects in pure STO ceramics were mainly V_{Ti}''' . The charge compensation mechanism of SLTO ceramics was predominantly formation of V_{Sr}'' . With increasing La content, ϵ_r of SLTO ceramics increased up to ~ 70000 at room temperature. The results of first-principle calculations indicated that the colossal permittivity came from a sharp polarization increase caused by dipole structure of defects. $\tan\delta$ of SLTO ceramics showed obvious Debye relaxation at high temperatures and the relaxation showed a multiple relaxation times derived from different kinds of polarization mechanism. The main polarization mechanism of SLTO ceramics gradually changed from ion displacement polarization to defect dipole polarization influenced by the concentration of La dopants.

Key words: La-doped SrTiO_3 , microstructure, point defects, colossal permittivity

1. Introduction

Large numbers of dielectric materials have been used to miniaturize electronics even more, and they also have a lot of applications in high-energy-density storage because of their excellent performance, colossal permittivity (CP, $\epsilon_r > 10^3$) as well as very low dielectric loss. Thus, many researchers are still focusing on discovering new dielectric materials with high-performance [1,2]. Nowadays several mechanisms have been proposed, which can cause high permittivity [3-6], resulting in the discovery of new CP materials such as doped TiO_2 , BaTiO_3 and SrTiO_3 (STO) dielectric ceramics.

However, the exact mechanisms and explanations for generating CP are still unclear. Originally, it was thought that a new intrinsic polarization mechanism caused by electrical charge ordering and/or crystal structure might have relation with CP. Then, lots of research works have shown that a well-known extrinsic Maxwell-Wagner (MW) polarization, which is associated with inhomogeneous electrical properties between grains and grain boundaries, can generate CP under some circumstances [7-9].

For the origin of CP, there is another viewpoint, considered from the point defects and the defect-dipole theory. Recently, Hu et al. [10] prepared (Nb+In) co-doped TiO_2 rutile ceramics exhibiting CP ($> 10^4$) and low dielectric loss (mostly < 0.05) largely independent on temperature and frequency over a wide temperature range of 80-450 K. It was explained that Nb^{5+} and In^{3+} substitutes Ti^{4+} sites and generated large defect-dipole clusters, which contained highly localized electrons, leading to the outstanding dielectric properties of co-doped TiO_2 ceramics.

For $\text{Ba}_{0.95}\text{La}_{0.05}\text{TiO}_{3-x}$ materials, the origin of CP has also been explained by the interfacial polarization effect by mobile electrons in the grains and oxygen vacancies ($V_{\text{O}}^{\cdot\cdot}$) in the vicinity of grain boundaries [11]. While for another important CP candidate, STO, the origin of CP has been seldom investigated, and it is just explained by the extrinsic Maxwell-Wagner interfacial polarization or the intrinsic polar order induced in SrTiO_3 ceramics [12,13]. But Wang et al. [14] pointed out that for $\text{SrTiZr}_x\text{O}_3$ ceramics sintered in N_2 , the colossal permittivity ($>10^4$) and low dielectric loss (<0.01) could be attributed to the existence of $V_{\text{O}}^{\cdot\cdot}$ -related giant defect dipoles and caused by the localized hopping electrons.

STO is one kind of typical perovskite-structure oxides having a wide band gap of $E_g \sim 3.2$ eV. In early studies, donor doping to the Sr or Ti sites of STO-based ceramics could lead to superconducting, high dielectric, thermoelectric and other special physical properties [15-17]. It has been proved that Nb-doped STO ceramics sintered in air usually have high dielectric loss [18,19]. But recently Wang et al. [14,20] reported that Sm- and Zr-doped STO ceramics sintered in nitrogen atmosphere at high temperatures revealed CP and very low dielectric loss over a temperature range of $25\text{ }^\circ\text{C} \sim 200\text{ }^\circ\text{C}$. Shen et al. [21] reported that $\text{Re}_{0.02}\text{Sr}_{0.97}\text{TiO}_3$ (Re=La, Sm, Gd, Er) ceramics showed a high dielectric permittivity, which is about 10-15 times higher than that of pure STO, while the dielectric loss still remained lower than 0.03 at room temperature. But explanations of these exciting phenomena were not given in the article. The mechanisms for CP in STO based ceramics are still not fully understood.

Positron annihilation spectroscopy (PAS) provides a non-destructive method to

research the defect and electronic structures. It can bring out unique information of the materials such as the electron momentum distribution, and defect status by using positrons annihilation radiation in condensed matter [22]. Mackie et al. [23] studied vacancies in STO single crystals by positron-annihilation lifetime spectroscopy (PALS). The results showed that Sr vacancies (V_{Sr}'') were predominantly in Nb-doped, electron-irradiated and vacuum-annealed samples. For undoped crystals, the point defects were mainly Ti vacancies (V_{Ti}'''). However, scholars have different points on the defect structure of STO-based ceramics [24,25], and further research is needed. The development of PAS analysis technique gives us a possibility to explain the origin of CP from the point defect level.

In this paper, the point defects of $Sr_{1-x}La_xTiO_3$ ceramics were studied by PAS, and the chemical state of each element was analyzed by X-ray Photoelectron Spectroscopy (XPS). *Ab-initio* modeling of defects was employed for proper interpretation of experimental data. A comparative study on the dielectric properties of SLTO ceramics and pure STO ceramics was presented. The origin of CP was discussed within the defect chemistry theory from the point defect level.

2. Experimental details

Ceramics of $SrTiO_3$ and $Sr_{1-x}La_xTiO_3$ ($x=0.05, 0.075, 0.10$ and 0.125) were prepared by the conventional solid-state reaction method. The raw materials were reagent-grade $SrCO_3$, TiO_2 and La_2O_3 powders. Firstly, these raw materials were weighed in stoichiometric proportions and ball milled in ethanol for 12 h and zirconia

balls were used as grinding media. After drying, the mixtures were calcined at 1300 °C for 4 h in air, and ball milled for 12 h again. With polyvinyl alcohol (PVA) as binder, the powders were granulated and pressed into cylindrical pellets (Φ 12 mm \times 1.5 mm). To burn out the binder, the compacts were heated at 500 °C for 2 h. Then STO samples were sintered at 1300 °C, 1400 °C, 1500 °C and 1600 °C for 2 h in air, while SLTO samples were only sintered at 1600 °C for 2 h in air.

X-ray diffraction (XRD) and scanning electron microscopy (SEM) were used for analyzing the crystalline structure and microstructure of the sintered samples. The XRD studies were carried out on X'Pert PRO diffractometer (Panalytical). The SEM observations were performed on Quanta 600 scanning electron microscope (FEI).

For investigation of point defects, two complementary PA techniques were employed: (i) PALS which enables identification of point defects and determinate their concentrations [26-29] and (ii) coincidence Doppler broadening (CDB) which provides information about local chemical environment of defects [30]. PAS measurements use a ^{22}Na positron source deposited on a 2 μm thick Mylar foil, and the activity is \approx 1 MBq. The positron source was always sealed between two pieces of the sample.

A digital spectrometer described in Ref. [31] was employed for PALS measurements. Time resolution (full width at half-maximum of the resolution function) of the spectrometer is 145 ps. By using a maximum likelihood program, the positron lifetime spectra, containing at least 10^7 positron annihilation events, were decomposed [32]. Based on contribution to positron lifetime spectra, the source consisted of two

components whose lifetime is 1.5 ns and 368 ps, and relative intensity is 1% and 7%, representing contributions of positrons annihilating in the covering Mylar foil and inside the ^{22}Na source spot, respectively.

The CDB studies were carried out using a digital CDB spectrometer [33] equipped with two high-purity Ge detectors and characterized by the energy resolution of 0.9 keV at the annihilation line of 511 keV and the peak-to-background ratio higher than 10^5 . At least 10^8 annihilations were collected in each two-dimensional CDB spectrum. Subsequently, the CDB spectra were reduced into one-dimensional cuts representing the resolution function of the spectrometer and the Doppler broadened annihilation peak. Normalized Doppler broadened peaks were divided by the normalized peak for a well-annealed pure Ti reference sample.

The valence states of elements were detected by XPS on a spectrometer AXIS-ULTRA DLD (Kratos). For the dielectric measurements, the sintered ceramic samples were polished. Then the silver electrodes were painted on both sides of the polished ceramic samples, and heated at 500 °C for 15 min. The dielectric properties were evaluated with a precision impedance analyzer E4980A (Agilent) in a wide temperature range (25-400 °C) and frequency ranging from 100 Hz to 1 MHz.

3. *Ab-initio* calculations

Positron lifetimes were calculated using density functional theory (DFT) within so-called standard scheme [34]. In this approximation positron density is assumed to be everywhere vanishingly small and not affecting the bulk electronic structure. At

first electron density $n(\mathbf{r})$ in the material is solved without the positron. Subsequently, the effective potential for positron is constructed as

$$V_+(\mathbf{r}) = \phi(\mathbf{r}) + V_{corr}[n(\mathbf{r}), \nabla n(\mathbf{r})] \quad (1)$$

where $\phi(\mathbf{r})$ is the Coulomb potential produced by the charge distribution of electrons and nuclei and V_{corr} is the zero positron density limit of the electron-positron correlation potential [34].

The ground state positron wave function $\psi_+(\mathbf{r})$ was calculated by solution of a single particle Schrödinger equation

$$-\frac{1}{2}\nabla^2\Psi_+(\mathbf{r}) + V_+(\mathbf{r})\Psi_+(\mathbf{r}) = E_+\Psi_+(\mathbf{r}) \quad (2)$$

where E_+ is the positron ground state energy. The positron lifetime was determined from the expression

$$\tau = \pi r_e^2 c \int \Psi_+(\mathbf{r}) n(\mathbf{r}) \gamma[n(\mathbf{r}), \nabla n(\mathbf{r})] d\mathbf{r} \quad (3)$$

where r_e is the classical electron radius, c is the speed of light, and γ denotes the electron enhancement factor accounting for the pile-up of electrons at the positron site [34].

The electron-positron correlation, i.e. the correlation potential V_{corr} and the enhancement factor γ , were treated using two approaches:

(i) local density approximation (LDA) utilizing the parametrization by Boroński and Nieminen [35] and taking into account incomplete positron screening [36]. In this approach V_{corr} and γ depends only on the local electron density at the positron site.

(ii) generalized gradient approximation (GGA) using the approach introduced by Barbiellini et al. [37]. Within this approach V_{corr} and γ depends not only on the local

electron density but also on its gradient.

The electron density $n(\mathbf{r})$ was constructed by superposition of atomic electronic densities calculated by a relativistic atomic code [38]. This approach called atomic superposition neglects the charge transfer, but it is computationally feasible and can be used even for very large supercells retaining full 3-D geometry of the problem [39].

The momentum distribution of annihilating electron-positron pairs was calculated using the approach described in Refs. [40,41]. The electron-positron correlations were treated with the GGA approach. The contribution $\rho^{i,nl}(p)$ from the i -th atom and a shell characterized by principal and orbital quantum numbers n, l was calculated by the formula

$$\rho^{i,nl}(p) = 4\pi^2 r_e^2 c N^{i,nl} \gamma^{i,nl} \left| \int R_+^i(r) R_-^{i,nl}(r) B_l(pr) r^2 dr \right|^2 \quad (4)$$

where $N^{i,nl}$ denotes the number of electrons in the (n, l) shell, B_l is the spherical Bessel function and the symbols $R_-^{i,nl}$ and $R_+^i(r)$ denote the electron and positron radial wave functions. The symbol $\gamma^{i,nl}$ stands for the state-dependent positron enhancement factor [41]. The momentum distribution of the annihilating electron-positron pairs is obtained by summing the partial contributions $\rho^{i,nl}(p)$ over all occupied atomic sites and corresponding electron shells. Since core electrons localized in atomic shells are practically not affected by crystal bonding and retain their atomic character the present approach describes well the high momentum part of the momentum distribution where the contribution of positrons annihilated by core electrons dominates.

In order to mimic the effect of the finite resolution of the experimental setup, the theoretical momentum distribution curves were convoluted with a Gaussian with FWHM of $4.0 \times 10^3 m_0 c$. The calculated momentum distributions are presented as ratio curves related to momentum distribution calculated for a perfect Al crystal.

The *ab-initio* calculations of positron lifetimes and momentum distributions of annihilating electron-positron pairs were performed for the perovskite STO structure with the lattice parameter $a=3.905 \text{ \AA}$. Lattice defects were modeled using $4 \times 4 \times 4$ 320-atom based supercells. Substitutional La defects were created by replacing corresponding number of Sr ions by La ones. Vacancies were formed by removing corresponding atoms from the supercell.

First-principle calculations were undertaken also to investigate the polarization strength and the formation energy of La substitution defects in STO. The latter was calculated by the following formula:

$$E_f = E_{(La-SrTiO_3)} - E_{(SrTiO_3)} - n\mu_{La} + n\mu_{Sr} \quad (5)$$

where $E_{(SrTiO_3)}$ and $E_{(La-SrTiO_3)}$ represent the total energies of a pure STO supercell and a supercell of the same size containing n La atoms substituting Sr ones. The symbols μ_{La} and μ_{Sr} represent the chemical potential of La and Sr (taken from the total energies of bulk metals). The calculations were performed by adopting the spin-polarized density function theory (DFT) method which considered spin-orbit interactions, as implemented in the Vienna ab-initio simulation package (VASP). The ion-electron interactions were calculated by the projector augmented plane-wave (PAW) method. The electronic exchange-correlation potential was calculated by the

Perdew-Burke-Ernzerhof (PBE) formula of generalized gradient approximation (GGA). The Brillouin zone integration was carried out by $2 \times 2 \times 2$ k-mesh based on the Monkhorst-Pack scheme. The cutoff energy for the plane wave basis expansion was set as 400 eV. The convergence criterion for the total energy calculations was set as 1×10^{-5} eV. All the atoms were fully relaxed until the force on every atom was smaller than 0.02 eV/Å.

Fig. 1 shows the lattice structure of STO. There are 135 atoms in $(3 \times 3 \times 3)$ STO supercell used in the calculations of polarization and defect formation energies. La doped STO was modeled by substituting of two Sr atoms by two La atoms which corresponds to the composition $\text{Sr}_{0.926}\text{La}_{0.074}\text{TiO}_3$. The second substituted Sr atom can be at the nearest-neighbor, second nearest-neighbor and larger distance positions, which are denoted as 1, 2 and 3, as shown in the figure. Corresponding defect structures are denoted (0,1), (0,2) and (0,3).

4. Results and discussion

4.1. Microstructure of STO and SLTO ceramics

The XRD patterns of STO and SLTO ceramics sintered at 1600 °C for 2 h are shown in Fig. 2. Fig. 2(a) indicates that STO and SLTO ceramics consist of single phase with cubic perovskite structure, which belongs to the $Pm3m$ space group. Thus La^{3+} ions incorporated into the SrTiO_3 lattice. Details of the (111) diffraction peak are shown in Fig. 2(b). With La content increasing, the (111) peak shifts to a larger scattering angles with a step to the opposite direction when $x = 0.1$.

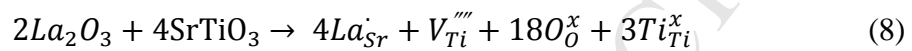
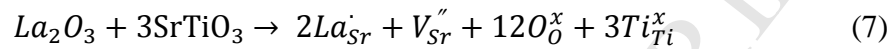
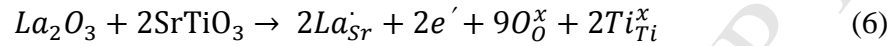
The lattice parameters (a) and cell volumes (V) obtained by the least square fitting of XRD patterns are shown in Table 1. The error range for a is -0.0003~0.0002 Å. As La doping content increases, the lattice parameter decreases from 3.9080 to 3.9028 Å. Because La ionic radius (0.106 nm) is smaller than Sr ions (0.112 nm), the lattice shrinks when La take the place of Sr. Theoretical and bulk densities are collected in Table 1 as well. The error range for bulk density is -0.02~0.01 g/cm³. The relative densities of STO and SLTO ceramics sintered at 1600 °C are all above 93%.

SEM images of STO and SLTO ceramics are shown in Fig. 3. The microstructure of the samples is homogeneous and grains packed closely. However, there are some visible small pores which in accordance with density of the samples slightly lower than the theoretical density. And the grain size of SLTO samples is remarkable smaller than that of STO samples. Hence, some of La addition can suppress the grain growth of SrTiO₃ during sintering. With La doping content increasing, the grains grow larger.

4.2. Point defects

Trivalent La ions substituted divalent Sr sites carry excess positive charges, to maintain electric neutrality, there are two different ways: one is by the formation of conducting electrons whose concentration is equal to that of the donor ions (electron compensation mechanism), and the other one is by the formation of V_{Sr}'' or V_{Ti}''' (vacancy compensation mechanism). Besides, for donor-substituted SrTiO₃, after sintering in reducing atmospheres, the titanium valence will change from Ti⁴⁺ to Ti³⁺ to ensure electrical neutrality [42]. Since the Ti³⁺ concentration equals to the charge

carrier density, this charge compensation method is also called electronic compensation [43], which leads to samples become semi-conductive. According to Kröger and Vink [44], the charge compensation mechanisms of La^{3+} doped SrTiO_3 can be expressed as the following formulas:



To make deeper study on the compensation mechanisms, STO and SLTO ceramics were investigated by PAS. Before SLTO ceramics can be discussed, the intrinsic defect structure of pure STO ceramics should be fully understood.

4.2.1 Results of positron lifetimes by *ab-initio* calculations

Table 2 collects the results of *ab-initio* calculations of positron annihilation lifetimes for various positron states in STO lattice. The calculated positron lifetimes depend on the approach used for the electron-positron correlation. The bulk positron lifetime τ_B , i.e. the lifetime of free positron delocalized in a perfect (defect-free) STO lattice calculated within the LDA and GGA approach is 131 and 151 ps, respectively. These values are in excellent agreement with the lifetimes calculated using the similar approach in Ref. [21]. The experimental bulk positron lifetime measured on Nb-doped STO single crystal was $\tau_B=141(1)$ ps [45]. This value falls into the range defined by LDA and GGA calculations.

It is known that the LDA approximation usually slightly overestimates the

positron annihilation rate and the calculated lifetimes are therefore slightly shorter than the experimental values while the lifetimes calculated by the GGA approach are often slightly higher than in the experiment [46]. Indeed, from inspection of Table 2 it is clear that lifetimes calculated using the LDA approach are lower than those obtained within the GGA scheme. Hence, the results calculated by the LDA and GGA approaches define the interval into which the actual lifetimes should fall. The differences between various approaches to the electron-positron correlation are to a large extent cancelled using ratios of the calculated lifetimes to the bulk lifetime τ_B calculated within the same scheme [37,39]. Hence, in comparison of experimental data with *ab-initio* calculations we always use ratio of the calculated lifetime to the bulk lifetime calculated with the same scheme, i.e. $\tau/\tau_{B,LDA}$ and $\tau/\tau_{B,GGA}$, multiplied by the experimental bulk lifetime $\tau_B=141$ ps. The lifetimes obtained in this way are listed in the last two columns of Table 2 and are indeed similar for both approaches.

The *ab-initio* calculations revealed that $V_O^{\ddot{}}$ is only a shallow positron trap unable to fully confine positron. This is demonstrated by calculated positron lifetime which is only a few ps longer than the bulk lifetime and also by negligible positron binding energy. On the other hand, cation vacancies ($V_{Sr}^{\prime\prime}$ and $V_{Ti}^{\prime\prime\prime}$) represent deep positron traps. Although isolated $V_O^{\ddot{}}$ does not trap positrons, $V_O^{\ddot{}}$ associated with a cation vacancy forming $V_{Sr}^{\prime\prime}+V_O^{\ddot{}}$ or $V_{Ti}^{\prime\prime\prime}+V_O^{\ddot{}}$ complex causes a considerable increase in the lifetime of trapped positron. Hence, although isolated $V_O^{\ddot{}}$ is not detectable by positrons, it can be seen when it forms complex with a cation vacancy.

More complex point defects were considered in the calculations as well, seen in

Fig. 4. Namely Shottky defect ($V_{Sr}''+V_{Ti}''' +3V_O\ddot{}$) maintaining the electrical neutrality and partial Shottky defects $V_{Ti}''' +2V_O\ddot{}$ and $V_{Sr}''+V_O\ddot{}$ which are electrically neutral as well. The lifetimes of positrons trapped at these defects reflect the net open volume available in each defect, i.e. the longest positron lifetime was obtained for the Shottky defect $V_{Sr}''+V_{Ti}''' +3V_O\ddot{}$.

To examine the effect of La substitution, we considered V_{Sr}'' with two neighboring Sr ions replaced by La ($La_{Sr}' +V_{Sr}'' +La_{Sr}'$) and V_{Ti}''' with four neighboring Sr ions replaced by La ($La_{Sr}' +La_{Sr}' +V_{Ti}''' +La_{Sr}' +La_{Sr}'$). One can see in Table 2 that substitution of Sr ions by La has only a minor impact on lifetimes of trapped positrons.

4.2.2 PALS investigations of STO ceramics

Two exponential components well describes the positron lifetime spectra of STO samples sintered at different temperatures, with lifetimes τ_1 , τ_2 and normalized relative intensities I_1 , I_2 ($I_1+I_2=100\%$). The development of lifetimes of both components is plotted in Fig. 5 as a function of the sintering temperature. Both the lifetimes τ_1 and τ_2 measured in STO ceramic samples are significantly higher than τ_B . It indicates that the defect density in STO ceramic samples is very high and almost all positrons are trapped at defects (so called saturated positron trapping). Type of defects in STO ceramics can be identified from comparison of the experimental data with theoretical calculations in Table 2. A dominating contribution of positrons trapped in V_{Ti}''' is the shorter component whose lifetime is $\tau_1 \approx 180$ ps. The longer component whose lifetime

is $\tau_2 \approx 300$ ps represents a contribution of positrons trapped at larger point defects making up of several vacancies. The most probable candidates for these defects are Shottky defects $V_{Sr}'' + V_{Ti}''' + 3V_O^\bullet$ characterized by the calculated lifetime in the range of 295-306 ps.

With increasing sintering temperature, τ_2 gradually decreases towards the lifetime for V_{Sr}'' and this is accompanied by a decrease in I_2 . Hence, the open volume of defects responsible for the component τ_2 becomes smaller and their concentration decreases. It indicates filling of V_O^\bullet by oxygen diffusing into the sample during sintering in air and decomposition of Shottky defects to V_{Ti}''' and V_{Sr}'' .

4.2.3 PALS investigations of SLTO ceramics

The results of PALS investigations for La-doped STO samples sintered at 1600 °C are plotted in Fig. 6. The PALS spectra of SLTO ceramics again are composed by two components with lifetimes τ_1 and τ_2 . The contribution of positrons trapped at V_{Ti}''' is the shorter component whose lifetime is $\tau_1 \approx 180$ ps, and the longer component represents Shottky defects whose lifetime is $\tau_2 \approx 300$ ps. With increasing content of La dopants, the intensity I_2 has a sharply increase. While when $x > 0.05$, the lifetime τ_2 decreases gradually towards the value of V_{Sr}'' .

These results demonstrate that the number of V_{Sr}'' increases with increasing La content. In SLTO ceramics V_{Sr}'' is the major defects, while the main defect in STO samples is V_{Ti}''' . The positive charge of La_{Sr} ions in SLTO need to be compensated, so V_{Sr}'' created and the concentration increases strongly. Hence, the PALS results

indicate that the vacancy compensation mechanism described by Eq. (7) is dominating in SLTO samples. La doping introduces V_{Sr}'' , and it can couple with La_{Sr}^{\cdot} to form electrically neutral defects $La_{Sr}^{\cdot}+V_{Sr}''+La_{Sr}^{\cdot}$. As one can see in Table 2, two La_{Sr}^{\cdot} ions in the neighboring sites of V_{Sr}'' have little influence on the lifetime of positrons trapped in V_{Sr}'' .

4.2.4 CDB investigations

The momenta information of electrons which annihilated positrons is included in the annihilation radiation, whose Doppler broadening can extract this information. The result of Doppler measurement gives the one-dimensional momentum distribution of the annihilating electron-positron pairs. In this electron-positron momentum distribution, the chemical environment where the annihilation event took place is characterized by the high-momentum part [40].

Fig. 7 shows the calculated CDB ratio curves for a perfect STO crystal and pure elements Sr, Ti, O and La. There are two characteristic features for the ratio curve of a perfect STO crystal: a peak at $p \approx 10 \times 10^{-3} m_0c$, which primarily from positron annihilations with 2p electrons of O but also comes from electrons belonging to Ti, Sr and La, and a broad peak at $p \approx 40 \times 10^{-3} m_0c$, coming from positrons annihilated in the vicinity of Ti ions.

The experimental CDB ratio curves with pure Al as reference for STO and SLTO ceramics sintered at 1600 °C are given in Fig. 8, and the ratio curves for pure Ti and Al_2O_3 standards are also plotted. Since pure Al is the reference, the shape of

the ratio curve for O can be estimated by the ratio curve for Al_2O_3 . Comparing Fig. 7 with Fig. 8, results of the calculated CDB ratio curves for Ti, O and STO are consistent with experiment qualitatively.

The shapes of CDB ratio curves for SLTO ceramics is similar with the STO sample, shown in Fig. 8, but the peak at $p \approx 10 \times 10^{-3} \text{ m}_0\text{c}$ is lower, indicating smaller contribution of positrons annihilated in the vicinity of O.

Fig. 9 shows the calculated CDB ratio curves for various defects in STO lattice. Since Ti ions are located in the center of oxygen octahedrons in STO lattice, V_{Ti}''' is surrounded by 6 oxygen ions and the O ions locate at the distance $a/2$ (a is the lattice parameter). Hence, positrons trapped at V_{Ti}''' are mainly annihilated by O electrons, which is reflected by an evident peak at $p \approx 10 \times 10^{-3} \text{ m}_0\text{c}$ in the calculated CDB ratio curve for V_{Ti}''' , see Fig. 9. V_{Sr}'' is also surrounded by O anions, but the distance ($a/\sqrt{2}$) is longer. Consequently, the peak at $p \approx 10 \times 10^{-3} \text{ m}_0\text{c}$ is lower for V_{Sr}'' . Note that the CDB ratio curve for $\text{La}_{\text{Sr}} + V_{\text{Sr}}'' + \text{La}_{\text{Sr}}$ is almost the same as that for V_{Sr}'' . For positrons trapped in Shottky defects, the contribution of positrons annihilated by O electrons is even lower than that for V_{Sr}'' since Shottky defect contains V_{O} . As a result, the CDB ratio curve calculated for Shottky defect exhibits the lowest peak at $p \approx 10 \times 10^{-3} \text{ m}_0\text{c}$.

Hence, the CDB results indicate that V_{Ti}''' is the predominantly defects in STO ceramics. When La^{3+} ion took place with Sr^{2+} ion in the STO lattice, V_{Sr}'' is generated, and form $\text{La}_{\text{Sr}} + V_{\text{Sr}}'' + \text{La}_{\text{Sr}}$ defect dipole structure. So it proves that in SLTO ceramics the vacancy compensation mechanism in equation (7) is predominant, in accordance with the PALS results.

4.2.5 XPS characterizations

There is another possible charge compensation mechanism that Ti^{4+} reduced to Ti^{3+} ($\text{Ti}^{4+} e$) because of trivalent La^{3+} ions displaced Ti sites carrying excess negative charges [47]. To examine this, the effect of La doping on the chemical structure of STO need to be evaluated using XPS. In XPS spectra the binding energies were calibrated by carbon ($\text{C } 1s = 284.6 \text{ eV}$). The full XPS spectra for STO and SLTO ceramics are shown in Fig. 10. The Sr $3s$, Sr $3p$, Sr $3d$, Sr $4s$, Ti $2s$, Ti $2p$, Ti $3s$, O KLL, O $1s$ and O $2s$ peaks can be observed clearly.

Fig. 11 gives the XPS spectra of La element for SLTO samples. The binding energy of La $3d_{5/2}$ and La $3d_{3/2}$ yields two peaks at 831.7 eV, 835.8 eV, 848.6 eV and 852.5 eV. This indicates that the oxidation state of La is 3+, and La atoms exist in two different compounds, which confirms that La atoms have entered into the SrTiO_3 lattice.

Fig. 12 gives the XPS spectra of Ti and Sr elements for STO and SLTO samples. For SLTO ceramics the binding energies of Ti $2p_{3/2}$ and Ti $2p_{1/2}$ are 458.81 eV and 464.61 eV, respectively corresponding to Ti with an oxidation state of 4+. The binding energy positions of Sr $3d_{5/2}$ and Sr $3d_{3/2}$ are 130.06 eV and 131.66 eV respectively, similar to that of Sr in SrF_2 [48,49]. Here, the component corresponds to α -Sr atoms having an oxidation state of 2+ in $\text{Sr}_{1-x}\text{La}_x\text{TiO}_3$ structure.

Besides, the positions of Ti $2p$ and Sr $3d$ shift to a higher binding energy of ~ 0.4 eV after doping La, due to the Fermi level becomes higher in SLTO ceramics [50].

The binding energies of Ti $2p$ and Sr $3d$ core levels for STO and $\text{Sr}_{0.875}\text{La}_{0.125}\text{TiO}_3$ ceramics are shown in Table 3. For STO and SLTO ceramics, the binding energy difference between Ti $2p_{1/2}$ and Ti $2p_{3/2}$ (ΔE -Ti $2p$) are 5.76 eV, 5.80 eV, respectively, and the binding energy difference between Sr $3d_{1/2}$ and Sr $3d_{3/2}$ (ΔE -Sr $3d$) are both 1.60 eV, in agreement with the results of literature [51]. There is no evidence that Ti^{4+} is reduced to Ti^{3+} , so the transformation from Ti^{4+} to Ti^{3+} because of La^{3+} -doping does not happen in SLTO ceramics. Hence, the XPS results indicate that the charge compensation in SLTO ceramics should be attributed to the formation of V_{Sr}'' , and La^{3+} doping increases the Fermi level.

4.3. Dielectric properties of STO and SLTO ceramics

The temperature dependence of the relative permittivity (ϵ_r) and the dielectric loss ($\tan\delta$) under 1 kHz for STO and SLTO ceramics are shown in Fig. 13. It can be seen that ϵ_r increases with increasing temperature, particularly after the temperature rising above 300 °C ϵ_r increases sharply for the $\text{Sr}_{0.875}\text{La}_{0.125}\text{TiO}_3$ sample.

At room temperature the dielectric properties of pure STO are $\epsilon_r = 300$ and $\tan\delta = 0.01$, consistent with the literature [52]. For SLTO ceramics ϵ_r increases with increasing La content. When La doping content $x = 0.125$, ϵ_r increased to 70000, which is 200 times higher than that of STO. Hence, the $\text{Sr}_{0.875}\text{La}_{0.125}\text{TiO}_3$ sample exhibits CP at room temperature. It is reasonable to assume that the origin of CP is closely related to the point defects structure in SLTO.

Table 4 compares the room-temperature dielectric properties of $\text{Sr}_{0.875}\text{La}_{0.125}\text{TiO}_3$

ceramics with the results of other high-permittivity compounds [1, 8, 10-12, 54]. These compounds all show unusual colossal dielectric constant. The highest value of $\sim 800,000$ was obtained for $\text{Ba}_{0.95}\text{La}_{0.05}\text{TiO}_{3-x}$, as well as the highest dielectric loss of ~ 0.7 . $\text{CaCu}_3\text{Ti}_4\text{O}_{12}$ ceramics show the best combination of high ϵ_r with relative low $\tan\delta$. However, the research work of intrinsic mechanisms for these compounds with colossal dielectric constant is still underway.

The defect formation energies and polarization values for La-doped STO and La-doped STO with Sr vacancy are calculated by *ab-initio* method, and the results are given in Table 5. The most energetically favorable configuration is the defect with structure (0,1) formed by two La atoms substituted two nearest Sr atoms. This structure is more stable by about 0.06 eV than the other two structures. For La-doped STO and La-doped STO with V_{Sr}'' , the calculated polarization value is $5.9 \mu\text{C}/\text{cm}^3$, $42.6 \mu\text{C}/\text{cm}^3$, respectively. Thus it is concluded that a sharp increase in polarization strength arises from the generation of V_{Sr}'' leading to CP in SLTO ceramics.

As discussed before, La^{3+} replacing Sr^{2+} sites carry excess positive charges and V_{Sr}'' formation is the predominant compensation mechanism to maintain the electric neutrality. The generation of V_{Sr}'' makes Ti-O octahedrons distort, and Ti^{4+} slightly deviates from the center position of the octahedron. This small displacement causes the dipole to reorient, contributing to the CP in SLTO ceramics [53]. In addition, the $\text{La}_{\text{Sr}} + V_{\text{Sr}}'' + \text{La}_{\text{Sr}}$ and Schottky defects will form defect dipoles with $V_{\text{O}}^{\bullet\bullet}$, which may exist in SLTO but cannot be detected by PALS, exacerbating the distortion of Ti-O

octahedrons and thus further improve the dielectric properties.

Fig. 14 shows the temperature dependence of ϵ_r and $\tan\delta$ for STO and SLTO ceramics under certain frequencies (100 Hz, 1 kHz, 10 kHz, 100 kHz and 1 MHz). As test frequency increases, the ϵ_r of all samples decreases, owing to the interface polarization relaxation and dipole orientation polarization relaxation. For STO ceramics, when the test temperature is lower 160 °C the ϵ_r increases gradually and then increases rapidly with temperature increasing further. The ϵ_r for $\text{Sr}_{0.95}\text{La}_{0.05}\text{TiO}_3$ sample has a similar tendency with STO ceramics. The $\tan\delta$ of STO ceramics shows a broad peak exhibiting frequency dispersion. For SLTO ceramics, when $x \geq 0.05$, the ϵ_r increases slowly as temperature increases. The dielectric loss peaks broaden with increasing La content.

From Fig. 14 we can see that, the test frequency range is 100 Hz-1 MHz, i.e. the time range of 10^{-2} - 10^{-6} s, which corresponds to the response time of the dipole orientation polarization. Based on the above analysis of defect types and charge compensation mechanisms, La^{3+} doping generates $\text{La}_{\text{Sr}}^{\bullet} + V_{\text{Sr}}'' + \text{La}_{\text{Sr}}^{\bullet}$ and Schottky point defects in STO. Cation vacancies (V_{Sr}'' , V_{Ti}''') and V_{O}^{\bullet} form defect dipoles with different response times. Thus with increasing La content, the concentration of defect dipoles increases and the relaxation phenomenon becomes more and more obvious.

Fig. 15 shows the frequency dependence of ϵ_r and $\tan\delta$ for STO and SLTO ceramics at different temperatures. For all samples, ϵ_r decreases rapidly as the frequency increases. When the frequency increases to a certain value f_T , ϵ_r becomes independent on temperature. The value of f_T is related with La doping content.

Dielectric loss peaks are clearly visible and display a dispersion that shifts to high frequency, exhibiting typical Debye relaxation behavior.

The test data of STO and SLTO ceramics were fitted by equation (9) [55-56] to calculate the value of β ($0 \leq \beta \leq 1$), which represents the degree of dispersion of relaxation time τ_0 .

$$\varepsilon^* = \varepsilon_\infty + \frac{\varepsilon_0 - \varepsilon_\infty}{1 + (i\omega\tau_0)^\beta} \quad (9)$$

As an example, when the test temperature is 280 °C, $\beta=0.98, 0.51, 0.85, 0.79, 0.79$, respectively. For STO ceramics, the value of β is close to 1, indicating that there is only an ion displacement polarization mechanism. For SLTO ceramics, the value of β becomes smaller, which means that the dispersion region is broader. When the La doping content is 0.05, β has the minimum value. According to the point defect analysis, when the La doping content is 0.05, there are intrinsic point defects, $La_{Sr}^{\cdot} + V_{Sr}'' + La_{Sr}^{\cdot}$ defects and Schottky point defects, so the ion displacement polarization and defect dipole polarization coexist. When the La doping content is more than 0.05, the polarization mechanism is mainly defect dipole polarization.

Federicci et al. [57] reported superionic conductor with colossal dielectric constant for $Rb_2Ti_2O_5$ materials annealed under oxygen-depleted atmosphere (such as He, N_2 , vacuum). They found that oxygen vacancies are created in the material, and the dielectric constant reaches unprecedented value of 10^9 . They proposed a possible mechanism of a Frenkel anionic defect. Additionally, they pointed out that another condition for the observation of such a high dielectric constant is that at least two ionic species of opposite signs are involved in the process. In this work, the charge

compensation mechanism of SLTO ceramics is predominantly the formation of V_{Sr}'' , resulting in $La_{Sr} \dot{+} V_{Sr}'' + La_{Sr} \dot{-}$ defect dipole structure, and Shottky defect ($V_{Sr}'' + V_{Ti}''' + 3V_O''$) coexists in the material. Thus there are two ionic species of opposite signs in SLTO ceramics, contributing to a high dielectric constant and dielectric relaxation.

To investigate the dielectric relaxation behavior, a powerful tool is activation energy analysis. The $\ln f_p$ versus $1/T$ plot was made and shown in Fig. 16. The variation relation obeys the Arrhenius relation:

$$f_p = f_0 \exp\left(-\frac{E_a}{k_B T}\right) \quad (10)$$

where f_p is the dielectric loss peak position, f_0 is the pre-exponential factor, E_a is the activation energy required for relaxation, k_B is the Boltzmann constant (1.38×10^{-23} J/K), and T is the absolute temperature. Applying logarithm on both sides of Eq. (10) the following relation can be obtained:

$$\ln f_p = \ln f_0 - \frac{E_a}{k_B T} \quad (11)$$

The development of frequencies of the dielectric loss peak with temperature for STO and SLTO ceramics is well described by Eq. (11) as demonstrated in Fig. 16. The E_a obtained from linear regression of the data for pure STO ceramic is about 1.12 eV, consistent with the result reported in literature (the E_a of STO single crystals is 1.15-0.80 eV) [50]. The dependence of E_a on La doping content for SLTO ceramics is plotted in Fig. 17. When $x \geq 0.075$, E_a decreased to ~ 0.25 eV. Choudhury [52] reported that this change in E_a seems to be connected with both the concentration and the mobility of the charge carriers which are apparently V_O'' in STO crystals. When

$x < 0.075$, intrinsic point defects become dominating type of defects and E_a increases with decreasing x up to 1.12 eV.

The relaxation time τ_0 is calculated by the following formula:

$$\tau_0 = \frac{1}{f_0} \quad (12)$$

The relaxation time τ_0 for STO and SLTO ceramics is plotted in Fig. 17 as function of x . From the values of τ_0 , the transformation of polarization mechanism can be deduced. For STO and $\text{Sr}_{0.95}\text{La}_{0.05}\text{TiO}_3$, the polarization mechanism belongs to the ion displacement polarization. When $x \geq 0.075$, the relaxation time prolongs indicating that the polarization mechanism changed to defect dipole polarization. It is believed that La^{3+} located at Sr^{2+} sites carry excess positive charges and the formation of $\text{La}_{\text{Sr}}^{\cdot} + V_{\text{Sr}}'' + \text{La}_{\text{Sr}}^{\cdot}$ defect dipole structure contributes to the improved polarization and increased relaxation time.

5. Conclusion

SLTO ceramics with colossal permittivity were fabricated by the conventional solid-state reaction method. The results of PALS and CDB indicated that intrinsic point defects in the pure STO ceramics are mainly V_{Ti}''' . The dominating charge compensation mechanism in SLTO ceramics is formation of V_{Sr}'' resulting in $\text{La}_{\text{Sr}}^{\cdot} + V_{\text{Sr}}'' + \text{La}_{\text{Sr}}^{\cdot}$ defect dipole structure. XPS results demonstrated that the transformation from Ti^{4+} to Ti^{3+} does not happen in La^{3+} -doped SLTO ceramics. As La doping content increases, ϵ_r of SLTO ceramics increases and shows colossal permittivity of ~ 70000 at room temperature. The colossal permittivity stems from a

sharp polarization increase caused by defect dipole structure. The $\tan\delta$ of SLTO ceramics showed obvious Debye relaxation at high temperatures and the relaxation showed a multiple relaxation times resulting from different kinds of polarization mechanism. The main polarization mechanism of SLTO ceramics gradually changes from the ion displacement polarization to the defect dipole polarization influenced by the concentration of La dopants.

Acknowledgements

This work was supported by the National Natural Science Foundation of China (No. 11372249, 51672219, 51702259), the International Cooperation Foundation of Shaanxi Province (No. 2017KW-025), the Research Fund of the State Key Laboratory of Solidification Processing (NWPU), China (No.137-QP-2015), and the “111” Project (No. B08040), and sponsored by Innovation Foundation for Doctor Dissertation of Northwestern Polytechnical University (No. CX201827). And the financial support by the Czech Science Foundation (No. P108/12/G043) is highly acknowledged. We would like to thank the Analytical & Testing Center of Northwestern Polytechnical University for the measurement of XRD, SEM and TEM.

References

- [1] C.C. Homes, T. Vogt, S.M. Shapiro, S. Wakimoto, A.P. Ramirez, Optical response of high-dielectric-constant perovskite-related oxide, *Sci.* 293 (2001) 673-676.
- [2] S. Krohns, P. Lunkenheimer, S. Meissner, A. Rellier, B. Gleich, A. Rathgeber, T.

- Gaugler, H.U. Buhl, D.C. Sinclair, A. Loidl, The route to resource-efficient novel materials, *Nat. Mater.* 10 (2011) 899-901.
- [3] N. Ikeda, H. Ohsumi, K. Ohwada, K. Ishii, T. Inami, K. Kakurai, Y. Murakami, K. Yoshii, S. Mori, Y. Horibe, H. Kito, Ferroelectricity from iron valence ordering in the charge-frustrated system LuFe_2O_4 , *Nat.* 436 (2005) 1136-1138.
- [4] M. Shu-Nan, M. Maki, Dielectric anisotropy in the charge-density-wave state of $\text{K}_{0.3}\text{MoO}_3$, *J. Phys. Soc. Jpn.* 80 (2011) 084706.
- [5] H.F. Hess, K. Deconde, T.F. Rosenbaum, G.A. Thomas, Giant dielectric constants at the approach to the insulator-metal transition, *Phys. Rev. B* 25 (1982) 5578-5580.
- [6] C.C. Wang, L.W. Zhang, Surface-layer effect in $\text{CaCu}_3\text{Ti}_4\text{O}_{12}$, *Appl. Phys. Lett.* 88 (2006) 042906.
- [7] D.C. Sinclair, T.B. Adams, F.D. Morrison, A.R. West, $\text{CaCu}_3\text{Ti}_4\text{O}_{12}$: One-step internal barrier layer capacitor, *Appl. Phys. Lett.* 80 (2002) 2153-2155.
- [8] T.B. Adams, D.C. Sinclair, A.R. West, Giant barrier layer capacitance effects in $\text{CaCu}_3\text{Ti}_4\text{O}_{12}$ ceramics, *Adv. Mater.* 14 (2002) 1321-1323.
- [9] M. Li, A. Feteira, D.C. Sinclair, Origin of the high permittivity in $(\text{La}_{0.4}\text{Ba}_{0.4}\text{Ca}_{0.2})(\text{Mn}_{0.4}\text{Ti}_{0.6})\text{O}_3$ ceramics, *J. Appl. Phys.* 98 (2005) 084101.
- [10] W.B. Hu, Y. Liu, R.L. Withers, T.J. Frankcombe, L. Noren, A. Snashall, M. Kitchin, P. Smith, B. Gong, H. Chen, J. Schiemer, F. Brink, J. Wong-Leung, Electron-pinned defect-dipoles for high-performance colossal permittivity materials, *Nat. Mater.* 12 (2013) 821-826.

- [11] S. Guillemet-Fritsch, Z. Valdez-Nava, C. Tenailleau, T. Lebey, B. Durand, J.Y. Chane-Ching, Colossal permittivity in ultrafine grain size BaTiO_{3-x} and $\text{Ba}_{0.95}\text{La}_{0.05}\text{TiO}_{3-x}$ materials, *Adv. Mater.* 20 (2008) 551-555.
- [12] A. Tkach, O. Okhay, A. Almeida, P.M. Vilarinho, Giant dielectric permittivity and high tunability in Y-doped SrTiO_3 ceramics tailored by sintering atmosphere, *Acta Mater.* 130 (2017) 249-260.
- [13] C. Liu, P. Liu, J.P. Zhou, Y. He, L.N. Su, L. Cao, H.W. Zhang, Colossal dielectric constant and relaxation behaviors in Pr: SrTiO_3 ceramics, *J. Appl. Phys.* 107 (2010) 094108.
- [14] Z.J. Wang, M.H. Cao, Q. Zhang, H. Hao, Z.H. Yao, Z.H. Wang, Z. Song, Y.M. Zhang, W. Hu, H.X. Liu, Dielectric relaxation in Zr-Doped SrTiO_3 ceramics sintered in N_2 with giant permittivity and low dielectric loss, *J. Am. Ceram. Soc.* 98 (2015) 476-482.
- [15] Y. Kozuka, M. Kim, C. Bell, B.G. Kim, Y. Hikita¹, H.Y. Hwang, Two-dimensional normal-state quantum oscillations in a superconducting heterostructure, *Nat.* 462 (2009) 487-490.
- [16] T. Sakudo, H. Unoki, Dielectric properties of SrTiO_3 at low temperatures, *Phys. Rev. Lett.* 26 (1971) 851-853.
- [17] H. Ohta, S.W. Kim, Y. Mune, T. Mizoguchi, K. Nomura, S. Ohta, H. Hosono, Giant thermoelectric Seebeck coefficient of a two-dimensional electron gas in SrTiO_3 , *Nat. Mater.* 6 (2007) 129-134.
- [18] J. Karczewski, B. Riegel, M. Gazda, P. Jasinski, B. Kusz, Electrical and

- structural properties of Nb-doped SrTiO₃ ceramics, *J. Electroceram.* 24 (2010) 326-330.
- [19] M.V. Raymond, V.R.W. Amarakoon, Microstructure and electrical properties of chemically prepared Nb₂O₅-doped SrTiO₃ ceramics, *J. Am. Ceram. Soc.* 73 (2005) 1308-1311.
- [20] Z.J. Wang, Z.H. Wang, M.H. Cao, Z.H. Yao, H. Hao, Z. Song, X.C. Huang, W. Hu, H.X. Liu, Structures and dielectric properties of Sr_{0.9775}Sm_{0.015}TiO₃ ceramics sintered in N₂, *Ceram. Int.* 41 (2015) 12945-12949.
- [21] Z.Y. Shen, Q.G. Hu, Y.M. Li, Z.M. Wang, W.Q. Luo, Y. Hong, Z.X. Xie, R.H. Liao, Structure and dielectric properties of Re_{0.02}Sr_{0.97}TiO₃ (Re=La, Sm, Gd, Er) ceramics for high-voltage capacitor applications, *J. Am. Ceram. Soc.* 96 (2003) 2551-2555.
- [22] R.W. Siegel, Positron annihilation spectroscopy, *Annu. Rev. Mater. Sci.* 10 (1980) 393-425.
- [23] R.A. Mackie, S. Singh, J. Laverock, S.B. Dugdale, D.J. Keeble, Vacancy defect positron lifetimes in strontium titanate, *Phys. Rev. B* 79 (2009) 014102.
- [24] A. Chen, Y. Zhi, Dielectric properties and defect structure in lanthanum doped SrTiO₃ ceramics, *J. Appl. Phys.* 71 (1992) 6025-6028.
- [25] B. Ullah, W. Lei, X.Q. Song, X.H. Wang, W.Z. Lu, Crystal structure, defect chemistry and radio frequency relaxor characteristics of Ce-Doped SrTiO₃ perovskite, *J. Alloy. Compd.* 728 (2017) 623-630.
- [26] F. Tuomisto, I. Makkonen, Defect identification in semiconductors with positron

- annihilation: experiment and theory, *Rev. Mod. Phys.* 85 (2013) 1583-1631.
- [27] L.H. Su, C. Lu, L.Z. He, L.C. Zhang, P. Guagliardo, A.K. Tieu, S.N. Samarin, J.F. Williams, H.J. Li, Study of vacancy-type defects by positron annihilation in ultrafine-grained aluminum severely deformed at room and cryogenic temperatures, *Acta Mater.* 60 (2012) 4218-4228.
- [28] A. Dupasquier, G. Kögel, A.Somoza, Studies of light alloys by positron annihilation techniques, *Acta Mater.* 52 (2004) 4707-4726.
- [29] R.E. Galindo, A.v. Veen, A.A. García, H. Schut, J.Th.M De Hosson, Study of polymer/metal coating under stress using positron annihilation spectroscopy, *Acta Mater.* 48 (2000) 4743-4747.
- [30] P. Asoka-Kumar, M. Alatalo, V.J. Ghosh, A.C. Kruseman, B. Nielsen, K.G. Lynn, Increased elemental specificity of positron annihilation spectra, *Phys. Rev. Lett.* 77 (1996) 2097-2100.
- [31] F. Becvar, J. Cizek, I. Prochazka, J. Janotova, The asset of ultra-fast digitizers for positron-lifetime spectroscopy, *Nucl. Instrum. Meth. Phys. Res. A.* 539 (2005) 372-385.
- [32] I. Prochazka, I. Novotny, F. Becvar, Application of maximum-likelihood method to decomposition of positron-lifetime spectra to finite number of components, *Mater. Sci. Forum.* 255-257 (1997) 772-774.
- [33] J. Cizek, M. Vlcek, I. Prochazka, Digital spectrometer for coincidence measurement of Doppler broadening of positron annihilation radiation, *Nucl. Instrum. Meth. Phys. Res. A* 623 (2010) 982-994.

- [34] M.J. Puska, R.M. Nieminen, Theory of positrons in solids and on solid surfaces, *Rev. Mod. Phys.* 66 (1994) 841-897.
- [35] E. Boroński, R.M. Nieminen, Electron-positron density-functional theory, *Phys. Rev. B* 34 (1986) 3820-3831.
- [36] M.J. Puska, S. Mäkinen, M. Manninen, R.M. Nieminen, Screening of positrons in semiconductors and insulators, *Phys. Rev. B* 39 (1989) 7666-7679.
- [37] B. Barbiellini, M.J. Puska, T. Korhonen, A. Harju, T. Torsti, R.M. Nieminen, Calculation of positron states and annihilation in solids: A density-gradient-correction scheme, *Phys. Rev. B* 53 (1996) 16201-16213.
- [38] J.P. Desclaux, A multiconfiguration relativistic DIRAC-FOCK program, *Comput. Phys. Commun.* 9 (1975) 31-45.
- [39] T. Korhonen, M.J. Puska, R.M. Nieminen, First-principles calculation of positron annihilation characteristics at metal vacancies, *Phys. Rev. B* 54 (1996) 15016-15024.
- [40] M. Alatalo, B. Barbiellini, M. Hakala, H. Kauppinen, T. Korhonen, M.J. Puska, K. Saarinen, P. Hautojärvi, R.M. Nieminen, Theoretical and experimental study of positron annihilation with core electrons in solids, *Phys. Rev. B* 54 (1996) 2397-2409.
- [41] J. Kuriplach, A.L. Morales, C. Dauwe, D. Segers, M. Šob, Vacancies and vacancy-oxygen complexes in silicon: Positron annihilation with core electrons, *Phys. Rev. B* 58 (1998) 10475-10483.
- [42] K. Uematsu, O. Sakurai, N. Mizutani, M. Kato, Electrical properties of La-doped

- SrTiO₃ (La: 0.1 to 2.0 at%) single crystals grown by xenon-arc image floating zone method, *J. Mater. Sci.* 19 (1984) 3671-3679.
- [43] J. Daniels, K.H. Härdtl, Electrical conductivity at high temperatures of donor-doped barium titanate ceramics, *Philips Res. Rep.* 31 (1976) 489-504.
- [44] F.A. Kröger, H.J. Vink, Relations between the concentrations of imperfections in crystalline solids, *Solid State Phys.* 3 (1956) 307-435.
- [45] A. Uedono, K. Shimoyama, M. Kiyohara, Z.Q. Chen, K. Yamabe, T. Ohdaira, R. Suzuki, T. Mikado, Vacancy-type defects in BaTiO₃/SrTiO₃ structures probed by monoenergetic positron beams, *J. Appl. Phys.* 91 (2002) 5307.
- [46] J.M. Campillo Robles, E. Ogando, F. Plazaola, Positron lifetime calculation for the elements of the periodic table, *J. Phys.: Condens. Matter* 19 (2007) 176222.
- [47] M.J. Akhtar, Z.U.N. Akhtar, R.A. Jackson, C.R.A. Catlow, Computer simulation studies of strontium titanate, *J. Am. Ceram. Soc.* 78 (1995) 421-428.
- [48] D. Ehre, H. Cohen, V. Lyahovitskaya, I. Lubomirsky, X-ray photoelectron spectroscopy of amorphous and quasicrystalline phases of BaTiO₃ and SrTiO₃, *Phys. Rev. B* 77 (2008) 184106-1-6.
- [49] S. Fuentes, P. Muñoz, N. Barraza, E. Chávez-Ángel, C.M. Sotomayor Torres, Structural characterisation of slightly Fe-doped SrTiO₃ grown via a sol-gel hydrothermal synthesis, *J. Sol-Gel Sci. Technol.* 75 (2015) 593-601.
- [50] T. Higuchi, T. Tsukamoto, N. Sata, M. Ishigame, Y. Tezuka, S. Shin, Electronic structure of p-type SrTiO₃ by photoemission spectroscopy, *Phys. Rev. B* 57 (1998) 6978-6983.

- [51] C.D. Wagner, W.M. Riggs, L.E. Davis, J.F. Moulder, G.E. Muilenberg (Ed.), Handbook of X-ray Photoelectron Spectroscopy (1st ed.), Perking-Elmer Corporation, Physical Electronics Division, Eden Prairie (1979) end of the book.
- [52] B.K. Choudhury, K.V. Rao, R.N.P. Choudhury, Dielectric properties of SrTiO₃ single crystals subjected to high electric fields and later irradiated with X-rays or y-rays, J. Mater. Sci. 24 (1989) 3469-3474.
- [53] Y. Zhi, A. Chen, P.M. Vilarinho, P.Q. Mantas, J.L. Baptista, Dielectric relaxation behaviour of Bi:SrTiO₃: III. Dielectric properties in the temperature range of 300-600 K, J. Eur. Ceram. Soc. 18 (1998) 1629-1635.
- [54] A.P. Ramirez, M.A. Subramanian, M. Gardela, G. Blumberg, D. Li, T. Vogt, S.M. Shapiro, Giant dielectric constant response in a copper-titanate, Solid State Commun., 115 (2000) 217-220.
- [55] A.K. Jonscher, Dielectric relaxation in solids[M]. Chelsea Dielectrics Press, London (1983) 96-101.
- [56] Junxin Fang, Zhiwen Yin (Ed.), Dielectric Physics[M], Science Press, Beijing (2000) 47-50.
- [57] Rémi Federicci, Stéphane Holé, Aurelian Florin Popa, Luc Brohan, Benoît Baptiste, Silvana Mercone, Brigitte Leridon, Rb₂Ti₂O₅: Superionic conductor with colossal dielectric constant, Phys. Rev. Mater. 1 (2017) 032001-1-6.

Figure list

- Fig. 1. Lattice structure of $(3 \times 3 \times 3)$ STO supercell with 135 atoms. The red spheres, green spheres and gray spheres represent O atoms, Sr atoms and Ti atoms, respectively. The labels 0, 1, 2 and 3 denote the position of Sr ion substituted by La.
- Fig. 2. (a) XRD patterns of STO and SLTO ceramics sintered at 1600 °C, (b) detail of (111) reflection.
- Fig. 3. SEM images taken in the cross section of ceramics sintered at 1600 °C. (a) SrTiO₃, (b) Sr_{0.95}La_{0.05}TiO₃, (c) Sr_{0.925}La_{0.075}TiO₃, (d) Sr_{0.9}La_{0.1}TiO₃ and (e) Sr_{0.875}La_{0.125}TiO₃.
- Fig. 4. The schematic depiction of defects in SLTO ceramics. (a) $La_{Sr}^{\cdot} + La_{Sr}^{\cdot} + V_{Ti}^{\prime\prime\prime} + La_{Sr}^{\cdot} + La_{Sr}^{\cdot}$, (b) $La_{Sr}^{\cdot} + V_{Sr}^{\prime\prime} + La_{Sr}^{\cdot}$, (c) Schottky defect ($V_{Sr}^{\prime\prime} + V_{Ti}^{\prime\prime\prime} + 3V_{O}^{\cdot\cdot}$).
- Fig. 5. Results of PALS investigations of STO ceramics sintered at various temperatures T_s : the development of (a) the lifetimes τ_1 , τ_2 of the components resolved in PALS spectra; (b) relative intensity I_2 of the longer component. The range of positron lifetimes $\frac{\tau}{\tau_{B,LDA}} \tau_B$, $\frac{\tau}{\tau_{B,GGA}} \tau_B$ obtained from *ab-initio* calculations for various defects ($V_{Ti}^{\prime\prime\prime}$, $V_{Sr}^{\prime\prime}$, Schottky defect) are shown by horizontal bands in Fig. 5a.
- Fig. 6. Results of PALS investigations of SLTO ceramics sintered at 1600 °C: (a) lifetimes τ_1 , τ_2 of the components resolved in PALS spectra; (b) relative intensity I_2 of the longer component plotted as a function of La content x . The range of positron lifetimes $\frac{\tau}{\tau_{B,LDA}} \tau_B$, $\frac{\tau}{\tau_{B,GGA}} \tau_B$ obtained from *ab-initio* calculations for various defects ($V_{Ti}^{\prime\prime\prime}$, $V_{Sr}^{\prime\prime}$, Schottky defect) are shown by horizontal bands in Fig. 6a.
- Fig. 7. Calculated CDB ratio curves (related to pure Al) for perfect STO crystal and Sr, Ti, O and La elements.

Fig. 8. The CDB ratio curves (related to pure Al) for STO and SLTO ceramics. The CDB curves for pure Ti and Al_2O_3 are plotted in the figure as well.

Fig. 9. The calculated CDB ratio curves (related to Al) for a perfect STO lattice and for various defects.

Fig. 10. XPS spectra of STO and SLTO ceramics sintered at 1600 °C. (a) SrTiO_3 , (b) $\text{Sr}_{0.95}\text{La}_{0.05}\text{TiO}_3$, (c) $\text{Sr}_{0.925}\text{La}_{0.075}\text{TiO}_3$, (d) $\text{Sr}_{0.9}\text{La}_{0.1}\text{TiO}_3$, (e) $\text{Sr}_{0.875}\text{La}_{0.125}\text{TiO}_3$.

Fig. 11. La 3d XPS spectra of SLTO ceramics sintered at 1600 °C. (a) $\text{Sr}_{0.95}\text{La}_{0.05}\text{TiO}_3$, (b) $\text{Sr}_{0.925}\text{La}_{0.075}\text{TiO}_3$, (c) $\text{Sr}_{0.9}\text{La}_{0.1}\text{TiO}_3$, (d) $\text{Sr}_{0.875}\text{La}_{0.125}\text{TiO}_3$.

Fig. 12. Ti 2p and Sr 3d XPS spectra for STO and SLTO ceramics sintered at 1600 °C. (a) SrTiO_3 , (b) $\text{Sr}_{0.95}\text{La}_{0.05}\text{TiO}_3$, (c) $\text{Sr}_{0.925}\text{La}_{0.075}\text{TiO}_3$, (d) $\text{Sr}_{0.9}\text{La}_{0.1}\text{TiO}_3$, (e) $\text{Sr}_{0.875}\text{La}_{0.125}\text{TiO}_3$. Dotted lines indicate peak positions for the STO ceramic.

Fig. 13. Temperature dependence of the dielectric constant and the dielectric loss for STO and SLTO ceramics (the test frequency was 1 kHz).

Fig. 14. Temperature dependence of the dielectric constant and dielectric loss for STO and SLTO ceramics at different frequencies. (a) SrTiO_3 , (b) $\text{Sr}_{0.95}\text{La}_{0.05}\text{TiO}_3$, (c) $\text{Sr}_{0.925}\text{La}_{0.075}\text{TiO}_3$, (d) $\text{Sr}_{0.9}\text{La}_{0.1}\text{TiO}_3$, (e) $\text{Sr}_{0.875}\text{La}_{0.125}\text{TiO}_3$.

Fig. 15. Frequency dependence of the dielectric constant and dielectric loss for STO and SLTO ceramics at different temperatures. (a) SrTiO_3 , (b) $\text{Sr}_{0.95}\text{La}_{0.05}\text{TiO}_3$, (c) $\text{Sr}_{0.925}\text{La}_{0.075}\text{TiO}_3$, (d) $\text{Sr}_{0.9}\text{La}_{0.1}\text{TiO}_3$, (e) $\text{Sr}_{0.875}\text{La}_{0.125}\text{TiO}_3$.

Fig. 16. The Arrhenius plots of $\ln f_p$ versus $1/T$ for the loss peak of STO and SLTO ceramics.

Fig. 17. The dependence of the activation energy E_a and relaxation time τ_0 on La doping content x for pure STO and SLTO ceramics.

Table list

Table 1 The lattice parameter, cell volume, theoretical density, bulk density and relative density of

STO and SLTO ceramics sintered at 1600 °C.

Table 2 Results of *ab-initio* calculations of positron annihilation lifetimes for various positron

states in STO crystal lattice. Electron-positron correlation was treated within the LDA or

GGA approach. The calculated lifetimes τ divided by the bulk lifetime calculated within the

same approach, i.e. either $\tau_{B,LDA}$ or $\tau_{B,GGA}$, and multiplied by the experimental bulk lifetime

$\tau_B=141$ ps are listed in the last two columns.

Table 3 The binding energies of Ti 2*p* and Sr 3*d* core levels of STO and Sr_{0.875}La_{0.125}TiO₃

ceramics.

Table 4 Dielectric properties of Sr_{0.875}La_{0.125}TiO₃, CaCu₃Ti₄O₁₂, (In_{0.5}Nb_{0.5})_xTi_{1-x}O₂,

Ba_{0.95}La_{0.05}TiO_{3-x}, and Sr_{1-1.5x}Y_xTiO₃ at room temperature (1 kHz).

Table 5 Defect formation energies and polarization values of La-doped STO and La-doped STO

with Sr vacancy.

Table 1 The lattice parameter, cell volume, theoretical density, bulk density and relative density of

STO and SLTO ceramics sintered at 1600 °C.

Samples	a (Å)	V (Å ³)	Theoretical density (g/cm ³)	Bulk density (g/cm ³)	Relative density (%)
SrTiO ₃	3.9080	59.687	5.106	4.89	95.78
Sr _{0.95} La _{0.05} TiO ₃	3.9050	59.545	5.190	4.84	93.24
Sr _{0.925} La _{0.075} TiO ₃	3.9037	59.489	5.231	4.96	94.85
Sr _{0.9} La _{0.1} TiO ₃	3.9045	59.526	5.263	5.04	95.79
Sr _{0.875} La _{0.125} TiO ₃	3.9028	59.447	5.306	5.00	94.25

Table 2 Results of *ab-initio* calculations of positron annihilation lifetimes for various positron states in STO crystal lattice. Electron-positron correlation was treated within the LDA or GGA approach. The calculated lifetimes τ divided by the bulk lifetime calculated within the same approach, i.e. either $\tau_{B,LDA}$ or $\tau_{B,GGA}$, and multiplied by the experimental bulk lifetime $\tau_B=141$ ps are listed in the last two columns.

Positron state	LDA	GGA	LDA	GGA
	τ (ps)	τ (ps)	$\frac{\tau}{\tau_{B,LDA}} \tau_B$ (ps)	$\frac{\tau}{\tau_{B,GGA}} \tau_B$ (ps)
STO bulk	131	151	141	141
$V_{\ddot{O}}$	135	158	145	148
$V_{Ti}^{''''}$	160	194	172	180
$V_{Sr}^{''}$	239	278	257	259
$V_{Ti}^{''''}+V_{\ddot{O}}$	189	225	203	210
$V_{Sr}^{''}+V_{\ddot{O}}$	245	281	264	262
Shottky defect $V_{Sr}^{''}+V_{Ti}^{''''}+3V_{\ddot{O}}$	284	315	306	295
Sr partial Shottky defect $V_{Sr}^{''}+V_{\ddot{O}}$	214	246	264	264
Ti partial Shottky defect $V_{Ti}^{''''}+2V_{\ddot{O}}$	214	246	230	230
$La_{Sr}^{\cdot}+V_{Sr}^{''}+La_{Sr}^{\cdot}$	239	276	257	258
$La_{Sr}^{\cdot}+La_{Sr}^{\cdot}+V_{Ti}^{''''}+La_{Sr}^{\cdot}+La_{Sr}^{\cdot}$	158	190	171	178

Table 3 The binding energies of Ti $2p$ and Sr $3d$ core levels of STO and $\text{Sr}_{0.875}\text{La}_{0.125}\text{TiO}_3$ ceramics.

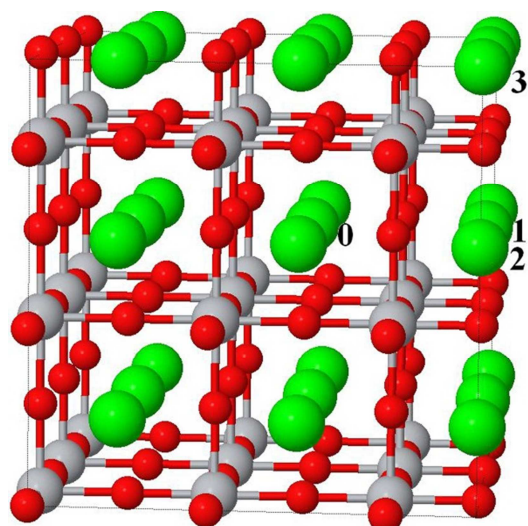
Samples	Line positions (eV)		
	STO	SLTO	ΔE
Ti $2p_{1/2}$	464.17	464.61	0.44
Ti $2p_{3/2}$	458.41	458.81	0.40
ΔE -Ti $2p$	5.76	5.80	--
Sr $3d_{3/2}$	131.26	131.66	0.40
Sr $3d_{5/2}$	129.66	130.06	0.40
ΔE -Sr $3d$	1.60	1.60	--

Table 4 Dielectric properties of $\text{Sr}_{0.875}\text{La}_{0.125}\text{TiO}_3$, $\text{CaCu}_3\text{Ti}_4\text{O}_{12}$, $(\text{In}_{0.5}\text{Nb}_{0.5})_x\text{Ti}_{1-x}\text{O}_2$, $\text{Ba}_{0.95}\text{La}_{0.05}\text{TiO}_{3-x}$, and $\text{Sr}_{1-1.5x}\text{Y}_x\text{TiO}_3$ at room temperature (1 kHz).

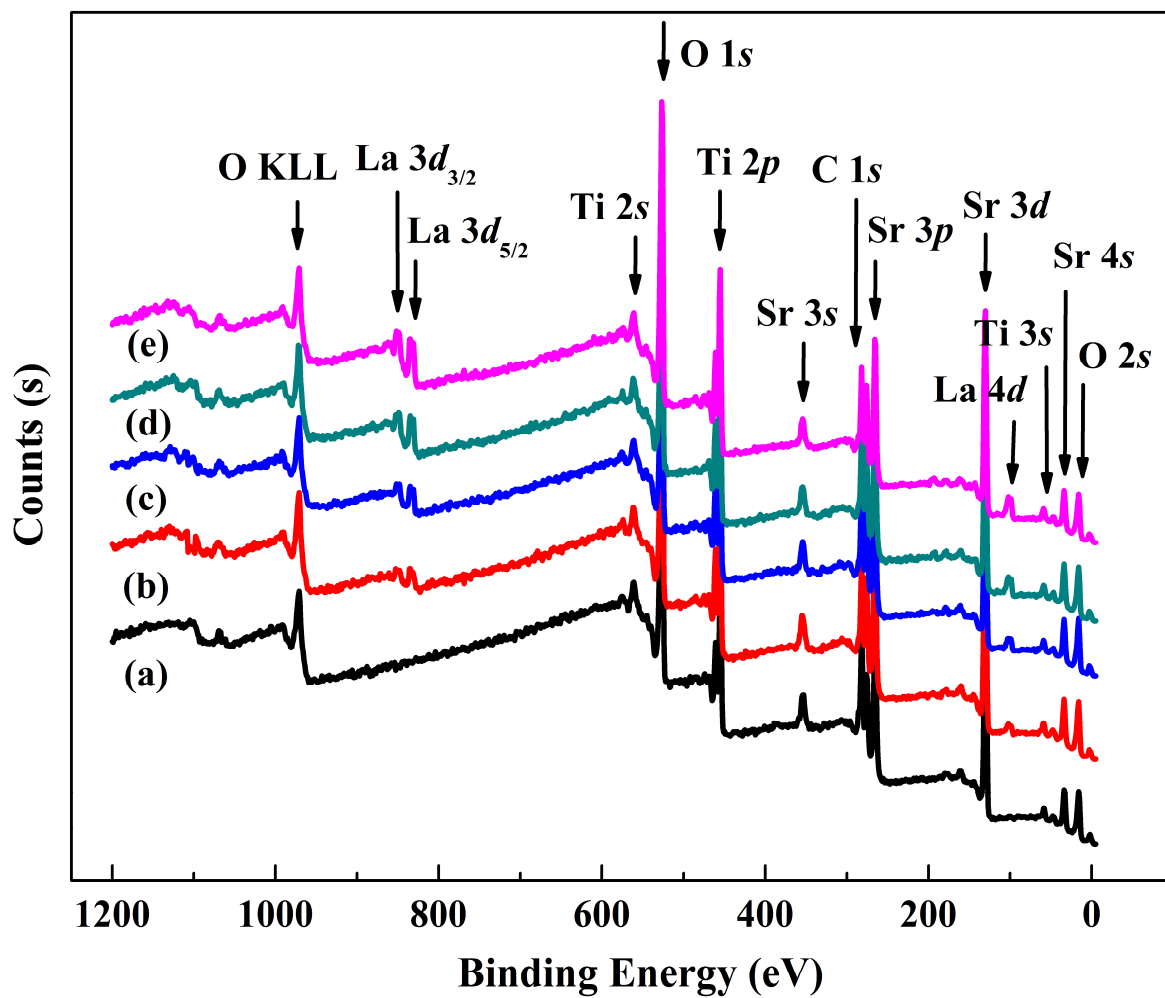
Ceramics composition	ϵ_r	$\tan\delta$	Ref.
$\text{CaCu}_3\text{Ti}_4\text{O}_{12}$	10,000-280,000	0.04-0.12	[1, 8, 54]
$(\text{In}_{0.5}\text{Nb}_{0.5})_x\text{Ti}_{1-x}\text{O}_2$	20,000-60,000	0.02-0.20	[10]
$\text{Ba}_{0.95}\text{La}_{0.05}\text{TiO}_{3-x}$	200,000-800,000	0.10-0.70	[11]
$\text{Sr}_{1-1.5x}\text{Y}_x\text{TiO}_3$	12,000~ 123,000	0.10-0.48	[12]
$\text{Sr}_{0.875}\text{La}_{0.125}\text{TiO}_3$	~ 70,000	0.30	This work

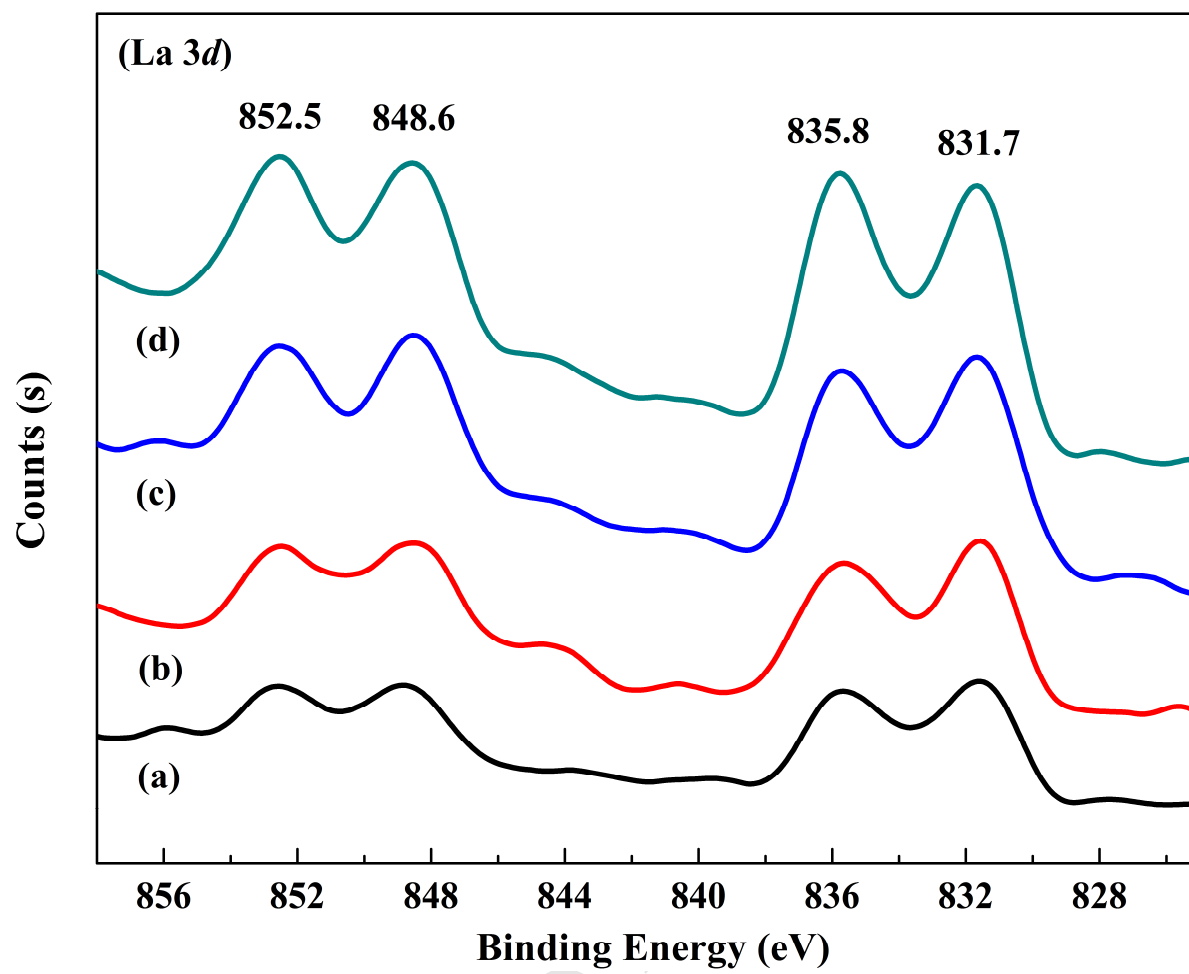
Table 5 Defect formation energies and polarization values of La-doped STO and La-doped STO with Sr vacancy.

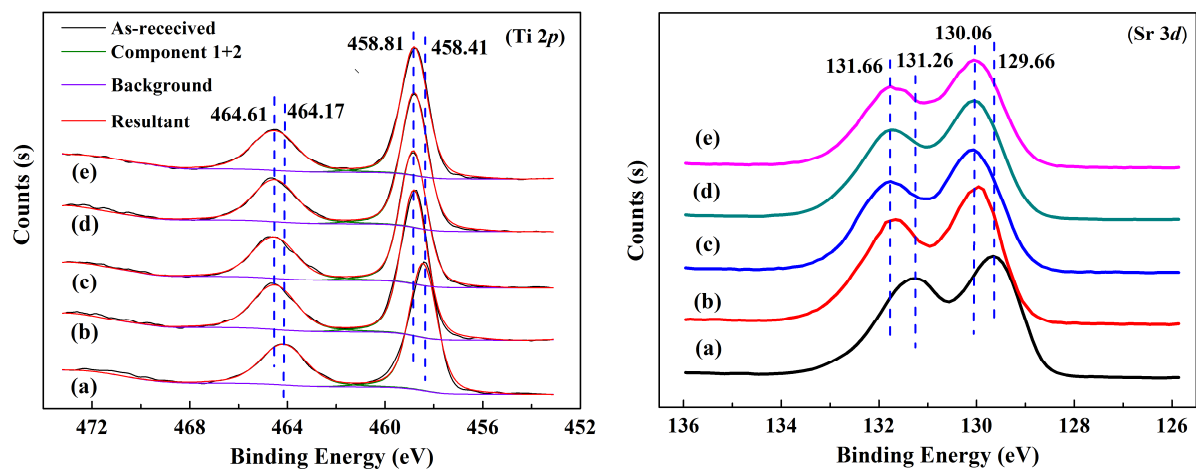
Compound	La-doped STO			La-doped STO with Sr vacancy		
	(0,1)	(0,2)	(0,3)	(0,1)	(0,2)	(0,3)
E_f (eV)	-2.82	-2.75	-2.76	1.19	1.28	1.20
P ($\mu\text{C}/\text{cm}^3$)	5.9	5.8	5.8	42.6	42.7	42.6

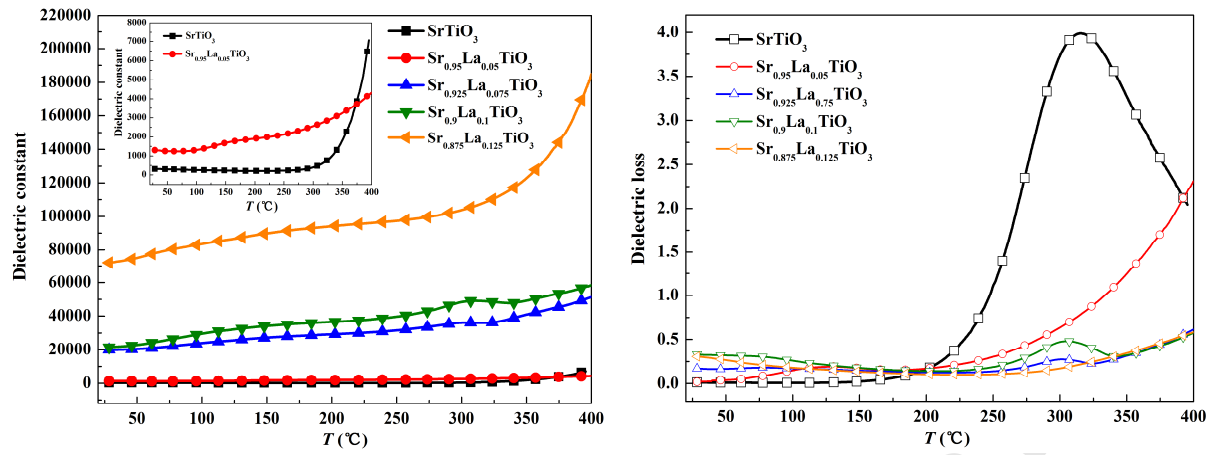


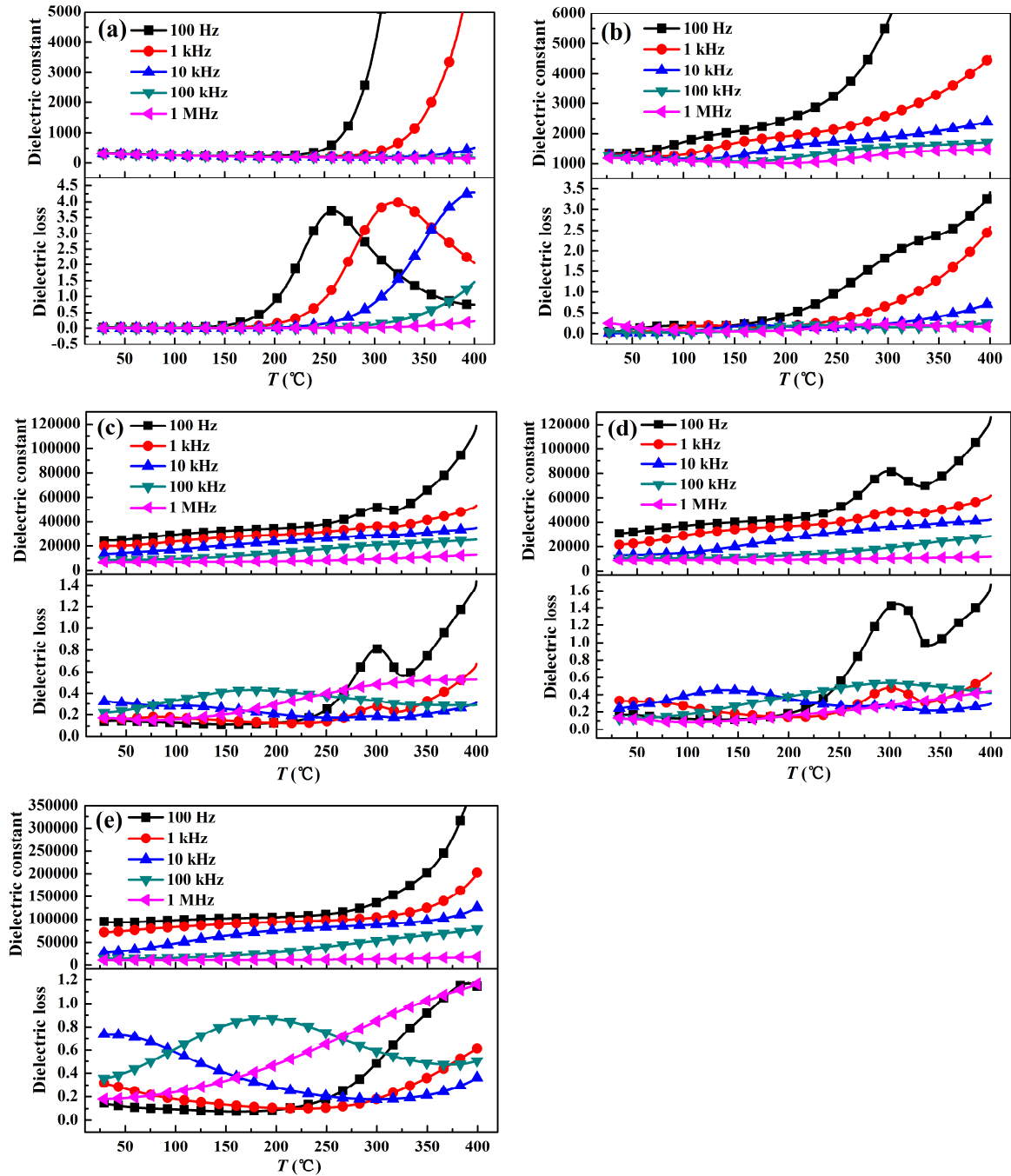
ACCEPTED MANUSCRIPT

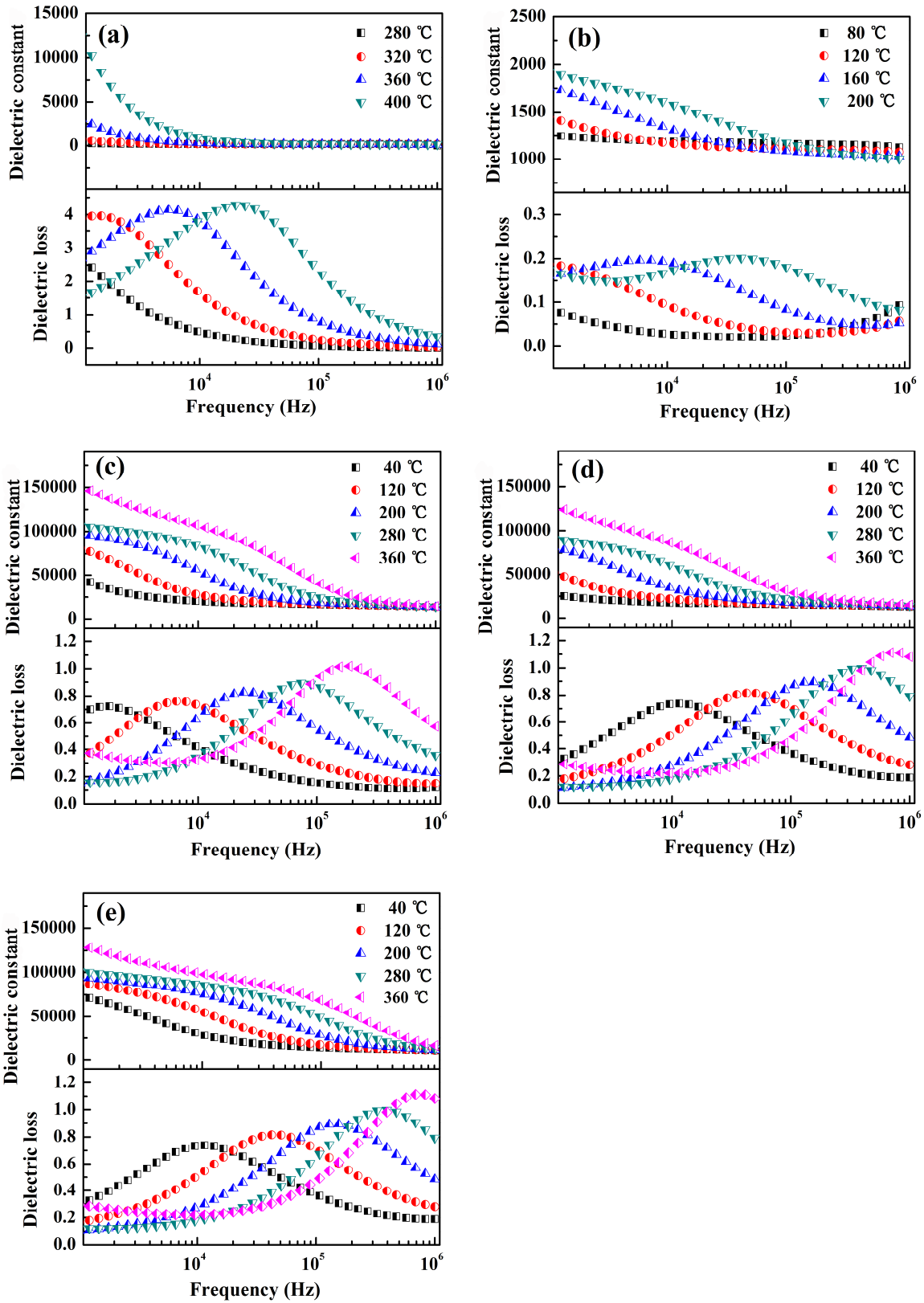


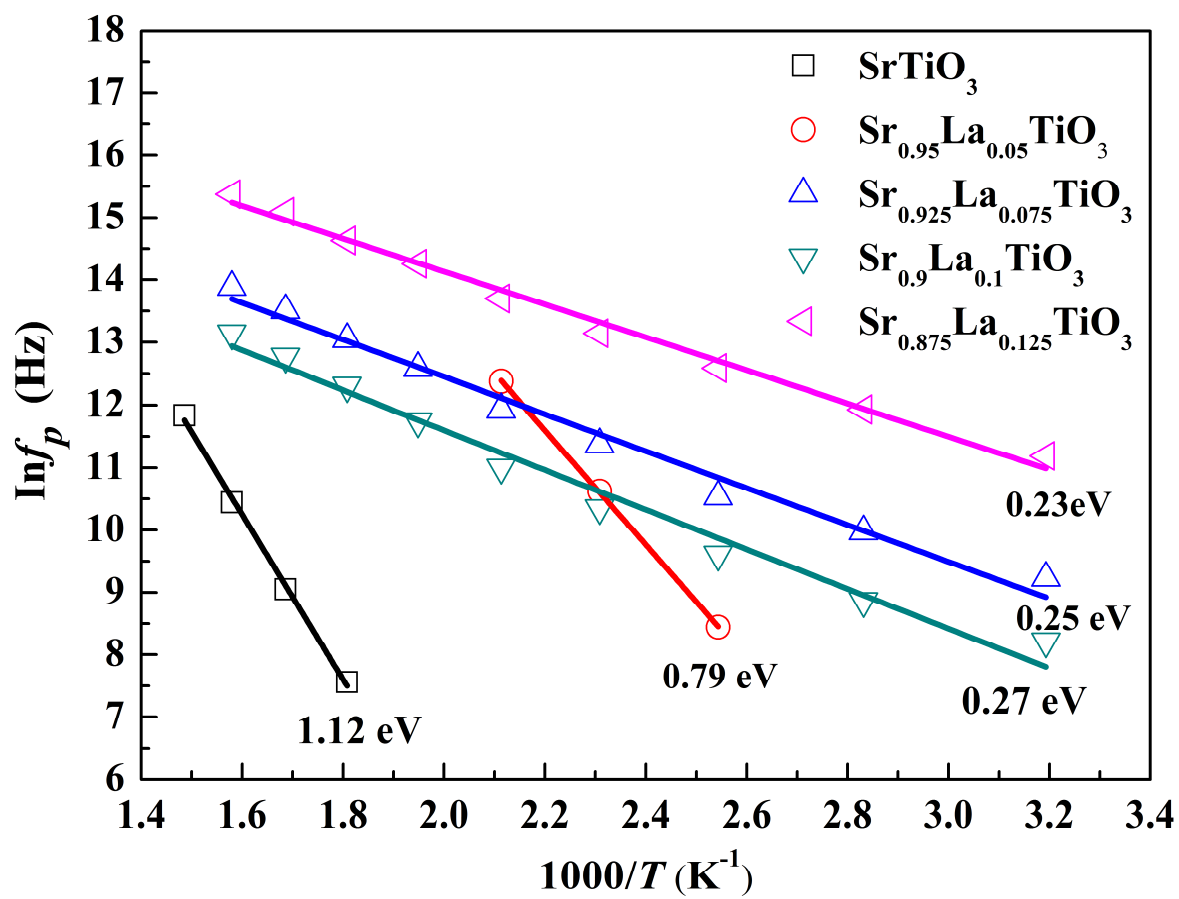


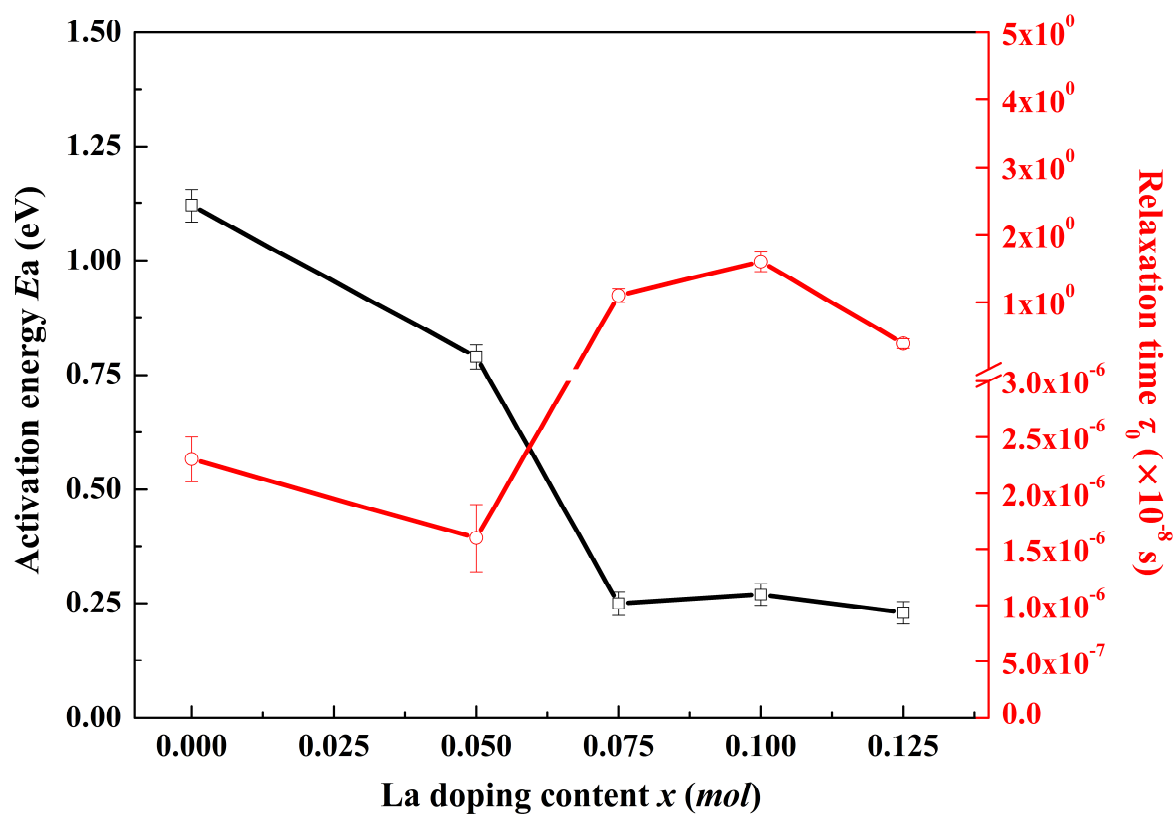


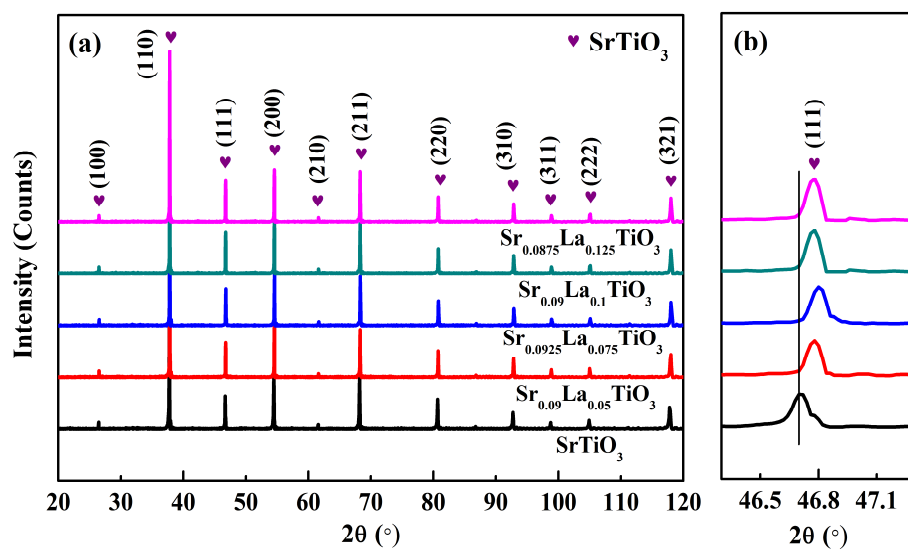


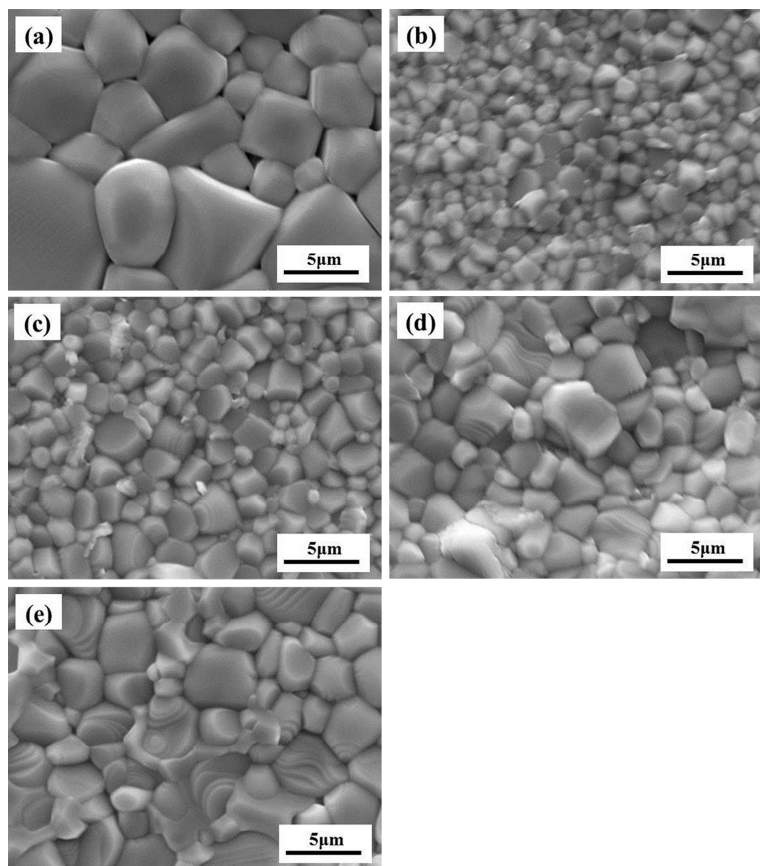


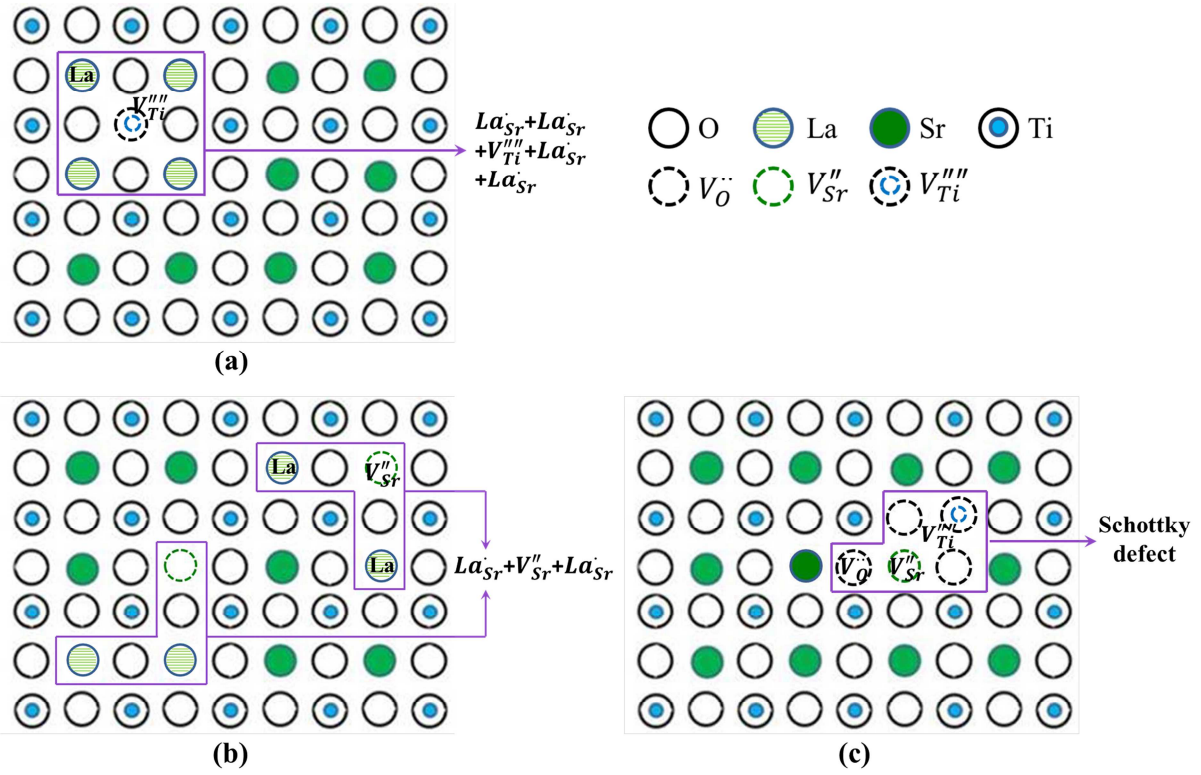












ACCEPTED MANUSCRIPT

